

## Article

# Magneto-Optical Imaging of Arbitrarily Distributed Defects in Welds under Combined Magnetic Field

Nvjie Ma <sup>1</sup>, Xiangdong Gao <sup>1,\*</sup>, Meng Tian <sup>1</sup>, Congyi Wang <sup>1</sup> , Yanxi Zhang <sup>1</sup>  and Perry P. Gao <sup>2</sup>

<sup>1</sup> Guangdong Provincial Welding Engineering Technology Research Center, Guangdong University of Technology, Guangzhou 510006, China; manvjie@gmail.com (N.M.); mengtian77@126.com (M.T.); wangcongyi126@126.com (C.W.); yanxizhang@126.com (Y.Z.)

<sup>2</sup> US-China Youth Education Solutions Foundation, New York, NY 10019, USA; perrygao99@gmail.com

\* Correspondence: gaofd@gdut.edu.cn

**Abstract:** Using the traditional magneto-optical detection methods, micro-weld defects parallel with the magnetic field direction may be overlooked. In order to overcome this, a non-destructive testing method based on magneto-optical imaging under a vertical combined magnetic field (VCMF) is proposed. To demonstrate this, the experimental results of the magneto-optical imaging of weld defects excited by a vertical combined magnetic field (VCMF) or parallel combined magnetic field (PCMF) are compared with those of traditional magnetic fields (constant magnetic field (CMF), alternating magnetic field (AMF), and rotating magnetic field (RMF)). It is found that the magneto-optical imaging under a VCMF can accurately detect weld defects of any shape and distribution. In addition, the center difference method is used to eliminate the influence of noise on the defect contour extraction of magneto-optical images, and the active contour of weld defects in the magneto-optical images is extracted. The results show that many noises can be identified by the robustness of the level set method, operating in low-pass filtering, so that much information that is usually lost can be retained.

**Keywords:** vertical combined magnetic field (VCMF); magneto-optical imaging; spot welding; image processing



**Citation:** Ma, N.; Gao, X.; Tian, M.; Wang, C.; Zhang, Y.; Gao, P.P.

Magneto-Optical Imaging of Arbitrarily Distributed Defects in Welds under Combined Magnetic Field. *Metals* **2022**, *12*, 1055.

<https://doi.org/10.3390/met12061055>

Academic Editor: Jean-Michel Bergheau

Received: 19 May 2022

Accepted: 18 June 2022

Published: 20 June 2022

**Publisher's Note:** MDPI stays neutral with regard to jurisdictional claims in published maps and institutional affiliations.



**Copyright:** © 2022 by the authors. Licensee MDPI, Basel, Switzerland. This article is an open access article distributed under the terms and conditions of the Creative Commons Attribution (CC BY) license (<https://creativecommons.org/licenses/by/4.0/>).

## 1. Introduction

With the development of science and technology, welding technology has been applied to various fields, such as the automobile industry, machinery manufacturing, the shipbuilding industry, aerospace, biomedicine, powder metallurgy, the microelectronics industry, energy generation, and other fields [1–3]. In the welding process, due to the influence of the weldment surface condition, joint gap [4], welding power [5], welding speed [6], and other factors, welded products are prone to welding defects, which directly affect the products' quality [7–9]. Spot welding is used to weld individual points on the contact surface of the weldment at the joint. In industrial production, spot welding is mainly used in the following aspects: (1) overlap in sheet metal stamping parts, (2) thin plate and section steel structures and skin structures, (3) screens, space frames, and cross steel bars, and so on [10,11]. In order to ensure the quality of products and projects, while avoiding accidents, non-destructive inspection of welds is required [12]. Common spot welding defects include excessively deep solder joints, partial burn-through, radial cracks, ring cracks, unwelded joints, black joints, distortion of solder joints, and shrinkage holes. The quality of the spot welding of the joint directly determines the mechanical properties of the products, so it is necessary to carry out non-destructive testing [13].

The non-destructive testing technology for spot welding is used to detect the weld nugget diameter and internal defects of the solder joint without damaging its performance. At present, there are three common detection methods at home and abroad. The first

method is based on the relationship among the electrode pressure, welding current, electrode displacement, and solder joint quality to predict the solder joint quality [14]. The second method is the solder joint failure test. The information of the joint strength and weld nugget diameter is obtained by destroying the solder joint, and the solder joint quality is evaluated according to the standard [14]. This is the most practical method in production at present, but this method not only has low efficiency, it also causes much material waste. The third method is to measure the voltage drop through the solder joint. The quality of the solder joint can be evaluated by converting the nugget diameter indirectly. This method has great application prospects and needs to be further studied. At present, the non-destructive testing methods of spot welding are radiographic testing [15], acoustic emission testing [16], ultrasonic testing [17–19], infrared thermography testing [20,21], dynamic resistance testing [22,23], eddy current testing [24,25], magnetic flux leakage testing [26,27], and so on.

In actual production, it is difficult to measure the difference in transmission intensity due to the composition of some metal materials and the characteristics of spot welding technology [15]. Moreover, because X-rays are harmful to the human body, the application of the radiographic inspection of solder joint quality in actual production is limited [15]. Many studies show that acoustic emission testing is only suitable for on-line detection and early damage prediction at present [16]. Due to the weak acoustic emission signal of some materials in actual production and the sound signal being easily affected by the environment, it is very difficult to detect the defects, and other detection methods are needed. Therefore, acoustic emission testing is only a supplementary means of detection and cannot replace the traditional detection method. Ultrasound cannot achieve high-quality imaging [28–31]. Eddy current flux leakage spot welding detectors can only detect surface defects, and the cost is high [24,25]. The dynamic resistance testing method only studies the non-destructive testing of the weld nugget diameter, and the relationship between the weld nugget diameter and solder joint quality needs to be further improved [22,23].

Because of its sensitivity to the change of magnetic field, the magneto-optical imaging detection method, as a new detection technology, has good detection results for welding defects [32]. The existing magneto-optical imaging technology has its own shortcomings. For example, under the CMF, the acquired magneto-optical images of welding defects contain limited information, and sometimes, some useful information of the welding defects will be lost. Dynamic magneto-optical images with more information can be obtained by the AMF. However, the detection results of micro-defects and subsurface defects are not good. Under the RMF, the magneto-optical image has a large amount of data, which is not suitable for on-line detection [33]. Although the paper mentioned that it could realize the visual imaging of multi-angle weld defects, during the test, it was found that, due to the limitation of the magnetic field intensity generated by the rotating magnetic field generator, if the defect is as small as a certain order of magnitude or located on the sub-surface, the quality of the magneto-optical image will be greatly reduced and even cannot be imaged. According to the imaging principle of the magneto-optical imaging sensor, only when the defect is perpendicular to the direction of the magnetic field, the defect in the magneto-optical image can be clearly imaged. The circumferential cracks and radial cracks in spot welding will be parallel with the direction of the magnetic field in the detection process, which will lead to missed detections. Reference [32] only theoretically discussed the optimization of the visual imaging effect of small defects under combined magnetic fields and did not realize the magneto-optical imaging detection of small weld defects at any position. In view of the shortcomings, this paper proposes a magneto-optical non-destructive imaging method under the VCMF.

## 2. Magneto-Optical Imaging of Spot Welding

### 2.1. Principle of Magneto-Optical Imaging

Based on the Faraday effect, magneto-optical imaging transforms the magnetic leakage field into a light intensity map to visualize defects [32,34]. That is, when the incident

polarized light  $I_0$  passes through the magnetic field, it will produce a rotation angle  $\theta$ . The polarized light  $I$  passing through the magneto-optical medium is proportional to the cosine of  $\theta$ . This rotation angle  $\theta$  and polarized light  $I$  can be expressed as

$$\theta = VBL \quad (1)$$

$$I = I_0 \cos \theta \quad (2)$$

where  $V$  (in radians per Tesla per meter) is the Verdet constant for the material and  $L$  is the propagation distance of the polarized light in the magnetic field.

Because the polarized light of the optical transmission line passes through the magneto-optical medium twice, the Faraday rotation angle of the polarization plane also rotates twice. In absence of an external magnetic field, the light intensity  $I$  detected by the polarizer can be expressed by Formula (3). When an external magnetic field is applied, the luminosity measured by the polarizer can be expressed as

$$I = I_0 \cos^2(2\alpha) \quad (3)$$

$$I = I_0 \cos^2(2(\alpha + \theta)) \quad (4)$$

where  $\alpha$  is the inherent rotational degree of the linear polarized light without an external magnetic field. The mean Faraday rotation angle of polarized light with the excitation of a magneto-optical film under a uniform magnetic field can be expressed as

$$\theta_F = \frac{\theta A^+ - \theta A^-}{A^+ + A^-} \quad (5)$$

where  $A^+$  and  $A^-$  are the effective domains corresponding to the magneto-optical image.

The rotation angle is different under different magnetic field strengths  $B$ . Each magneto-optical image can be represented as a matrix array of  $i \times j$ , in which the pixels of the  $i$ th row and  $j$ th column are represented as  $I_{ij}$ . The effective domain range corresponding to each pixel can be defined as  $A_{ij}^+$  and  $A_{ij}^-$ , and the corresponding average Faraday rotation angle  $\bar{\theta}_{ij}$  can be expressed as

$$\bar{\theta}_{ij} = \frac{\theta_{ij} A_{ij}^+ - \theta_{ij} A_{ij}^-}{A_{ij}^+ + A_{ij}^-} \quad (6)$$

where  $\theta_{ij}$  is the Faraday rotation angle caused by the positive effective domain corresponding to pixel  $I_{ij}$ .

Formulas (3) and (4) give the light intensity change under the corresponding Faraday rotation angle deflection. According to Formula (6), the distribution of each pixel of the magneto-optical image can be obtained, and the magneto-optical image  $I$  can be expressed as

$$I = \begin{bmatrix} I_{11} & I_{12} & \cdots & I_{1j} \\ I_{21} & I_{22} & \cdots & I_{2j} \\ \vdots & \vdots & \ddots & \vdots \\ I_{i1} & I_{i2} & \cdots & I_{ij} \end{bmatrix} \quad (7)$$

Therefore, the magneto-optical sensor forms magneto-optical images with different light intensities, that is magneto-optical imaging of welding defects.

However, for invisible defects, only when the defect is perpendicular to the excitation field is it easy to image. It is well known that spot welding is prone to circumferential and radial cracks. However, most of the exciting magnetic fields are double magnetic poles, which makes it difficult to ensure that all circumferential cracks or radial cracks in solder joints are perpendicular to the direction of the magnetic field. Therefore, there will

be missed detections. As shown in Figure 1a, the distribution of the magnetic field and crack in double-pole excitation is shown. It can be seen from Figure 1a that part of the radial crack and some circumferential cracks are parallel with the direction of the magnetic field. According to the principle of magneto-optical imaging, these cracks parallel with the magnetic line of force are difficult to image.

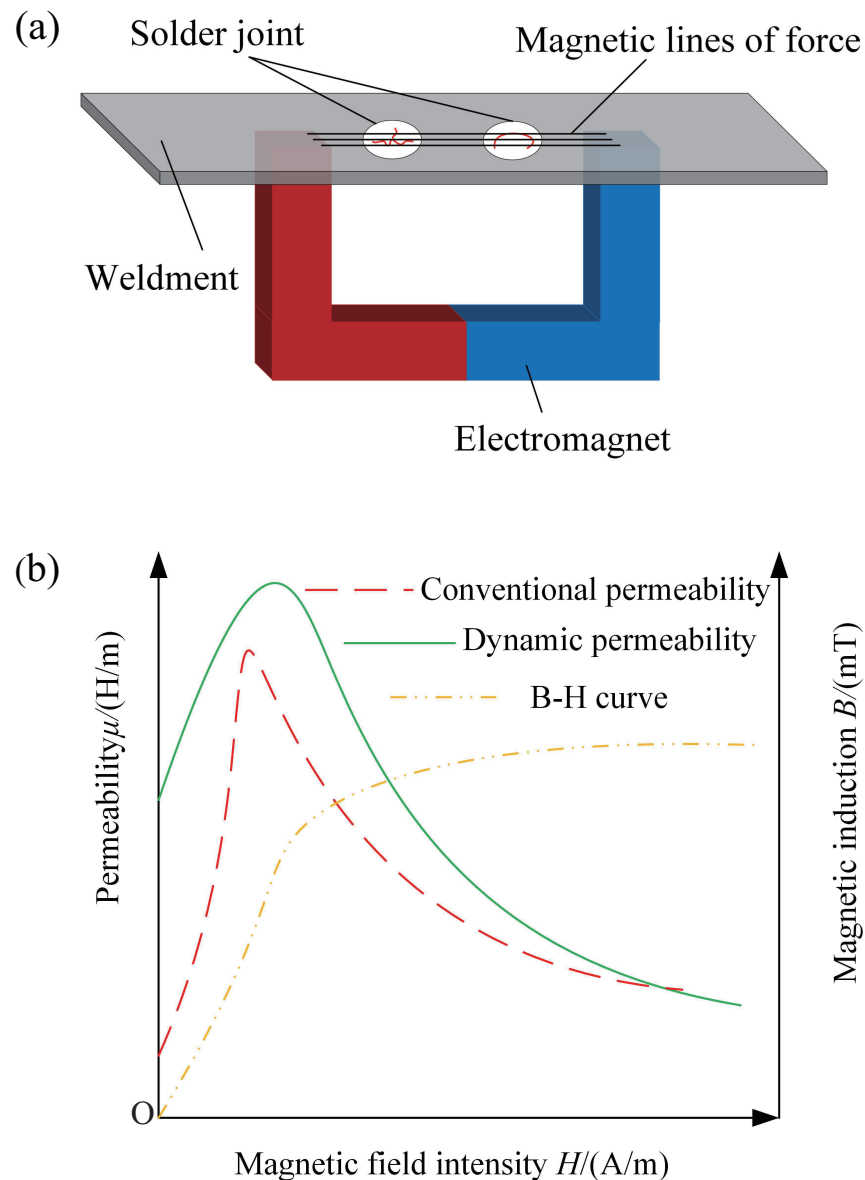


**Figure 1.** Excitation law. (a) Distribution diagram of the internal magnetic line of force of the weldment. (b) Change curve of permeability and magnetic induction intensity.

In ferromagnetic materials, the calculation formula of magnetic induction is as follows:

$$B = \mu M + \mu H \quad (8)$$

$$B \approx \mu H \quad (9)$$

where  $B$  denotes the mean of magnetic induction,  $\mu$  denotes permeability,  $M$  denotes magnetization, and  $H$  denotes magnetic field intensity. The variation trend of  $M$  with  $H$  is basically the same as that of  $B$  with  $H$ . Therefore, Equation (8) can be simplified to Equation (9). The magnetization law of ferromagnetic materials is represented by the curve of  $B$  and  $H$ , which is named the B-H curve, as shown in Figure 1b. The slope of

any point on the B-H curve connected to the origin  $o$  represents the permeability of the magnetized state. The permeability change curve of the ferromagnetic sample under the CMF is named conventional permeability. Therefore, the expression of permeability can be expressed by Equation (10). Equation (11) is obtained by differentiating the two sides of Equation (10). Then, according to the relationship between total differential and partial differential equation, the partial differential equation can be obtained by sorting out Equation (11), as shown in Equation (12).

$$\mu = \frac{B}{H} \quad (10)$$

$$d\mu = \frac{HdB - BdH}{H^2} \quad (11)$$

$$\frac{dB}{dH} = \frac{B}{H} + H \frac{d\mu}{dH} = \mu(H) + H \frac{d\mu(H)}{dH} \quad (12)$$

It can be seen from Figure 1b that with the increase of the magnetic field intensity, the magnitude of the magnetic induction first increases sharply, then remains stable. With the increase of the magnetic field intensity, the conventional permeability first increases sharply and then decreases rapidly. The appeal formula and image show that the change of the magnetic field intensity will affect the permeability and magnetic induction intensity. When the excitation field is the AMF, the permeability of the tested sample changes with time. This will also have an effect on the induced magnetic field. The dynamic permeability  $\mu_d$  is defined as follows:

$$\mu_d = \frac{1}{\mu_0} \frac{dB}{dH} \quad (13)$$

where  $\mu_0$  is the vacuum permeability, and its value is  $\mu_0 = 4\pi \cdot 10^{-7}$  H/m. From the right side of Formula (13), we can see that  $\mu_d$  is a univariate function of  $H$ , which can be denoted as  $\mu_d(H)$ . When the amplitude of the AMF is large, the sample will vibrate. This will affect the imaging effect of weld defect detection. Therefore, if the amplitude of the magnetization of the AMF is small, it can be approximately considered that the dynamic permeability of the internal hysteresis loop is basically unchanged. According to the definition of dynamic permeability, Formula (14) is approximately established.

$$\Delta B \approx \mu_0 \mu_d(\bar{H}) \Delta H \quad (14)$$

Through a comparative analysis of the conventional permeability and dynamic permeability curves in Figure 1b, it can be seen that under the combined magnetic fields, the defects of the tested samples are easier to obtain with a larger leakage magnetic field. Using this feature, the shortcomings of magneto-optical imaging under the AMF mentioned above will be effectively overcome. Based on the analysis, a non-destructive testing method of magneto-optical imaging under the excitation of the VCMF is proposed.

## 2.2. Magneto-Optical Imaging Experiment of Spot Welding

The test material for the laser spot welding was a medium carbon steel plate with a size of  $100 \times 200 \times 1$  mm. The physical picture of the polished test sample is shown in Figure 2. The labels of the solder joints on the samples are from 1 to 5. In the welding process, the defocus was 8 mm. The welding time was 1 s. The flow rate of the protective gas was 20 L/min. The laser power from labels 1 to 5 was 2 kW, 2.1 kW, 2.2 kW, 2.3 kW, and 2.4 kW, respectively. Two radial crack samples were detected by magneto-optical imaging. The schematic diagram of the magneto-optical imaging experimental platform is shown in Figure 2c.

The spot welding samples were tested under the CMF, AMF, RMF, PCMF, and VCMF. The parameters of the imaging test equipment are shown in Table 1. The schematic diagram of the magnetic pole position is shown in Figure 3. Under the six excitation conditions, as

shown in Figure 3, the magneto-optical imaging tests were carried out on crack 1 and crack 2, respectively.

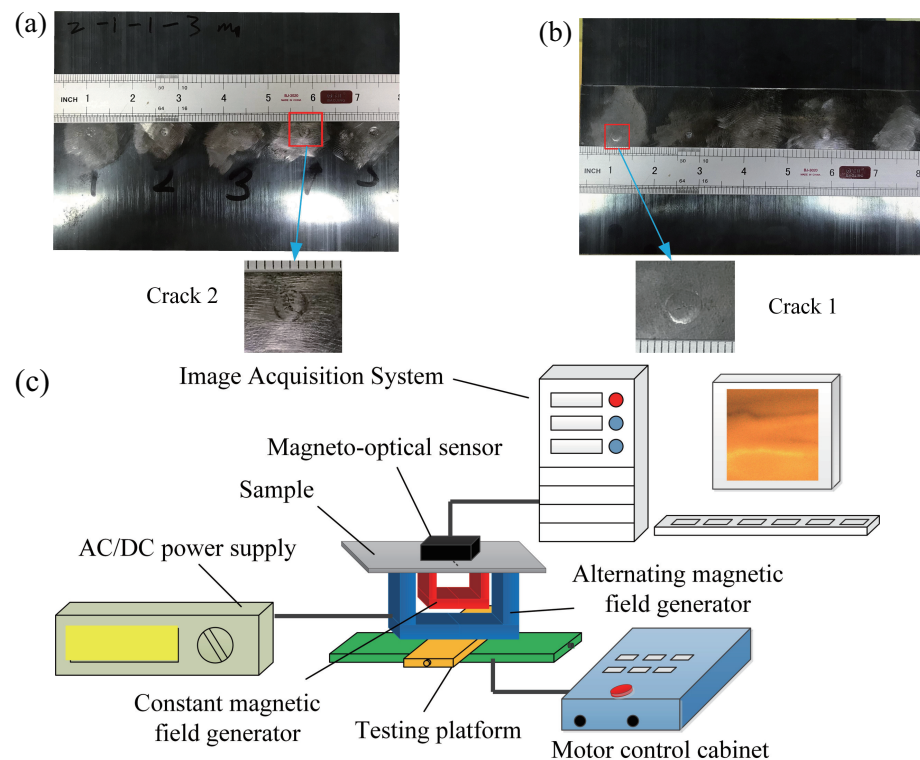


**Figure 2.** Experimental sample and schematic diagram of the platform. (a) Front of sample. (b) Back of sample. (c) Schematic diagram of experimental platform.

**Table 1.** Parameters of experimental equipment.

Equipment	Parameter	Numerical Value
CMF	Iron core	Ferrite
	Turn ratio	700
	Excitation source	DC
	Excitation value	0–1 V
	Lift-off value	0 mm
AMF	Iron core	Silicon steel sheets
	Excitation source	50 Hz AC
	Input value	0–220 V
	Excitation value	0–35 V
	Lift-off value	25 mm
RMF	Iron core	Silicon steel sheets
	Excitation source	50 Hz AC
	Input value	0–220 V
	Lift-off value	25 mm
Magneto-optical imaging sensor	Sampling frequency	75 frame/s
	Image pixel	400 × 400 pixel
	Sensor lift-off value	1 mm
	Window size	4 × 4 mm <sup>2</sup>

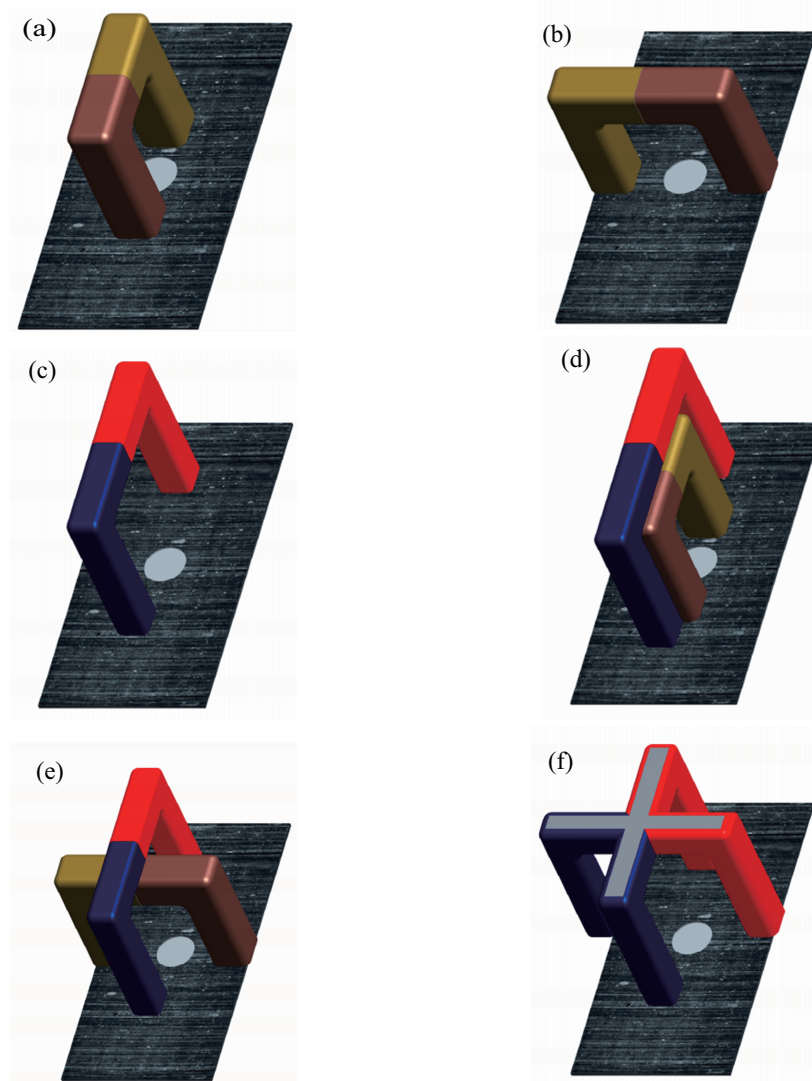


**Figure 3.** Position of magnetic poles in the magneto-optical imaging experiment. (a) Pole of CMF1. (b) Pole of CMF2. (c) Pole of AMF. (d) Pole of PCMF. (e) Pole of VCMF. (f) Pole of RMF.

During the magneto-optical imaging test, the voltage of the magnetic field excitation source and the lift-off degree of the magnetic pole are shown in Table 2. In the table, TN, V, and MF represent test number, value, and magnetic field, respectively. During the magneto-optical imaging test under the CMF, it was found that the magneto-optical image of the crack was saturated when the excitation source input was 1 V. Therefore, the magneto-optical image obtained when the excitation source input was 0.5 V was selected as the research object. In the process of magneto-optical imaging test under the AMF, the magneto-optical image of the crack was not clear when the excitation source input was small. Therefore, the magneto-optical image obtained when the excitation source input was 35 V was selected as the research object. Similarly, the magneto-optical image obtained when the excitation source input was 220 V was selected as the research object under the RMF. In order to compare and analyze the differences between the magneto-optical images of the welding defects under the different magnetic fields, the magneto-optical images obtained by the CMF excitation source of 0.5 V and the AMF excitation source of 35 V were selected as the research objects, whether it was the PCMF or the VCMF. The magneto-optical images of crack 1 and crack 2 are shown in Table 3.

**Table 2.** Parameters of magneto-optical imaging experiment.

		Crack 1					Crack 2						
CMF	Voltage (V)	0.5	0.5	1	-	-	CMF	Voltage (V)	0.5	0.5	-	-	-
	Lift-off (mm)	0	0	0	-	-		Lift-off (mm)	0	0	-	-	-
AMF	Voltage (V)	35	-	-	-	-	AMF	Voltage (V)	30	35	-	-	-
	Lift-off (mm)	25	-	-	-	-		Lift-off (mm)	25	25	-	-	-
PCMF	Voltage (V)	0.5	0.5	0.5	0.5	-	PCMF	Voltage (V)	0.5	0.5	0.5	0.5	0.5
	Lift-off (mm)	0	0	0	0	-		Lift-off (mm)	0	0	0	0	0
	Voltage (V)	20	25	30	25	-		Voltage (V)	35	15	20	25	30
	Lift-off (mm)	25	25	25	25	-		Lift-off (mm)	25	25	25	25	25
VCMF	Voltage (V)	0.5	0.5	0.5	0.5	1	VCMF	Voltage (V)	0.8	0.5	0.5	0.5	0.5
	Lift-off (mm)	0	0	0	0	0		Lift-off (mm)	0	0	0	0	0
	Voltage (V)	20	25	30	35	35		Voltage (V)	35	35	30	25	20
	Lift-off (mm)	25	25	25	25	25		Lift-off (mm)	25	25	25	25	25
RMF	Voltage (V)	220	-	-	-	-	RMF	Voltage (V)	220	-	-	-	-
	Lift-off (mm)	25	-	-	-	-		Lift-off (mm)	25	-	-	-	-

**Table 3.** Magneto-optical images of cracks obtained by experiments under different exciting magnetic fields.

MF	Crack 1			Crack 2		
CMF1						
CMF2						
AMF						
PCMF						
VCMF						
RMF						

It can be seen from Table 3 that, under a single CMF or AMF, the imaging of the radial cracks that are approximately perpendicular to the magnetic pole line is clear and the imaging of the radial cracks that are approximately parallel with the magnetic pole line is not clear, or even impossible. Under the PCMF, the imaging of the radial crack that is approximately perpendicular to the magnetic pole line is clearer under a single magnetic field. The imaging of the radial crack that is approximately parallel with the magnetic pole line is also unclear, or even impossible. Under the VCMF, multi-angle radial cracks can be imaged. Under the RMF, the multi-angle radial cracks on some magneto-optical images cannot be completely imaged, and some images are blurred.

### 3. Magneto-Optical Image Processing

#### 3.1. Analysis of Magneto-Optical Image Information

According to the magneto-optical imaging experiment in Section 2, the radial crack information contained in the magneto-optical image obtained under the VCMF is more

complete. The three frames of the magneto-optical imaging of radial crack comprise a period. The magneto-optical image is a true color image, which can be decomposed into three channels: R, G, and B. Therefore, each radial crack can obtain nine channel signal images. The original image, R-channel image, G-channel image, and B-channel image of the crack are shown in Figure 4. The gray value curve of column 257 of each image is also shown in Figure 4.

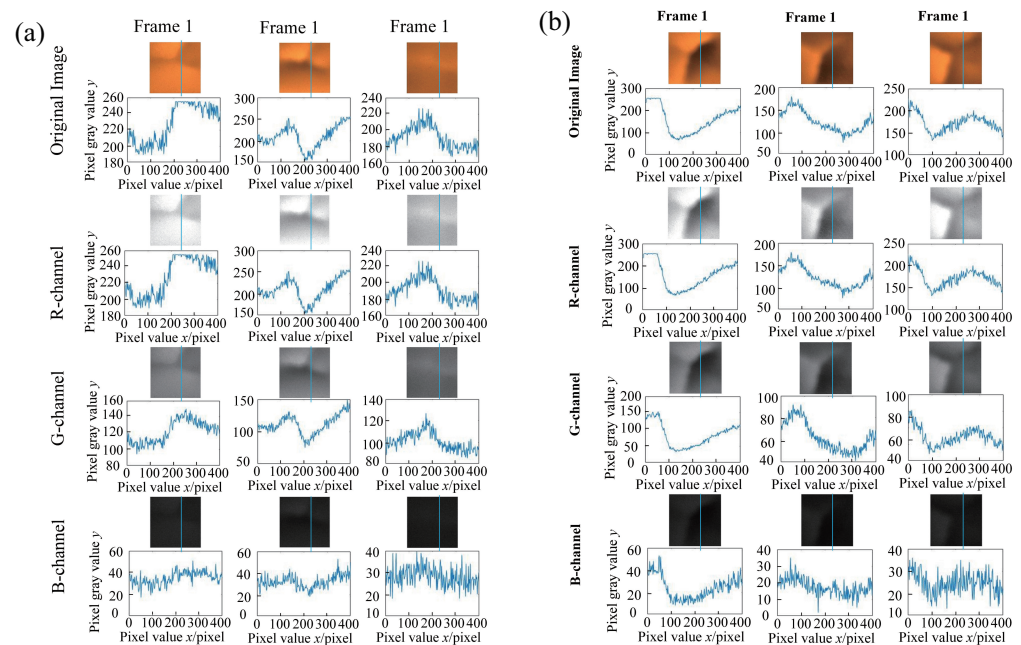


**Figure 4.** Each channel image and gray value curve of the original magneto-optical image. (a) Crack 2. (b) Crack 1.

As can be seen from Figure 4a,b, the gray value distribution of the R-channel is most similar to that of the original image. Therefore, when the original image is saturated, the R-channel image will also be saturated. For example, the first frame magneto-optical image and R-channel image of crack 1 and crack 2 have a saturation region (the gray value is 255). The gray value distribution range of the G-channel image shifts downward as a whole, but the length of the range is basically unchanged. In other words, the G-channel image can not only avoid image saturation effectively, but also reflect the contour information of defects on the magneto-optical image. The B-channel images are dark, and the gray value is less than 100. Most of the contour information of the gray value curve is not obvious, and the noise interference is large. By analyzing the gray value distribution range, line shape, and maximum gray value of the image, the G-channel image of the second frame of the magneto-optical image of crack 1 was selected as the research object to extract the contour of the weldment defects.

The components of the image whose gray intensity changes sharply (such as noise and object edge) exist in the high-frequency band. Slowly changing components (such as object shape and background) exist in the low-frequency band. The required information can be obtained by suppressing and retaining the specified frequency band. The Fourier transform was performed on the second frame of magneto-optical image of crack 1 and its G-channel image, and the spectrum diagram is shown in Figure 5. For image processing, the two-dimensional discrete Fourier transform formula is as follows:

$$F(u, v) = \sum_{x=0}^{i-1} \sum_{y=0}^{j-1} f(x, y) e^{-j2\pi(ux/i+vy/j)} \quad (15)$$

where  $f(x, y)$  is the gray value of the spatial variable  $(x, y)$  of the magneto-optical image with size  $i \times j$ .  $(u, v)$  represents the frequency domain variable.  $u$  is taken in the range of

$0, 1, 2, \dots, i - 1$ , and  $v$  is taken in the range of  $0, 1, 2, \dots, j - 1$ . It can be seen from Figure 5 that the boundaries of the high-frequency signal and low-frequency signal distribution regions of both the original magneto-optical image and the G-channel image are fuzzy. This is not conducive to welding defect contour extraction.

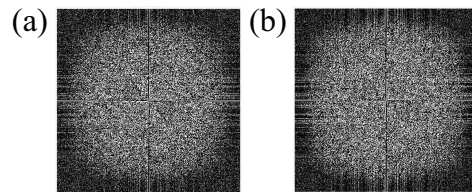


**Figure 5.** Spectrum of crack 1. (a) Spectrum of original image. (b) Spectrum of G-channel image.

### 3.2. Contour Extraction of Welding Defects

The quality of different channel information in the color magneto-optical images generated by the magneto-optical imaging sensor was analyzed. It was found that the gray level of the “dark area” and “bright area” was uneven in the original magneto-optical image. Therefore, the image with extrema can be obtained by deriving the gray value of the image along different directions. In image processing, the gray value is discrete, so the difference operation was used to approximate the derivative. The first-order difference operation includes the forward difference, backward difference, and central difference. The calculation formula is as follows:

$$A_x = \frac{A(x+h) - A(x)}{h} \quad (16)$$

$$A_x = \frac{A(x) - A(x-h)}{h} \quad (17)$$

$$A_x = \frac{A(x+h) - A(x-h)}{2h} \quad (18)$$

where  $A$  is the function value of the discrete function and  $h$  is the step size.

When the magnetization direction of the measured workpiece is perpendicular to the direction of the crack defect, the image with an extreme value in the middle of the crack defect can be obtained by calculating the partial conductance of the gray value of the magneto-optical image along the magnetization direction. In this paper, the detection sample has a multi-angle crack, so the X-direction and Y-direction center difference operation was carried out on the research object, respectively.  $h = 1$  is often used in image processing. Therefore, the center difference of the magneto-optical image is as follows:

$$A_x(x, y) = \frac{A(x+1, y) - A(x-1, y)}{2} \quad (19)$$

$$A_y(x, y) = \frac{A(x, y+1) - A(x, y-1)}{2} \quad (20)$$

where  $A_y(x, y), A_x(x, y), A(x+1, y), A(x-1, y), A(x, y+1), A(x, y-1)$  is the gray intensity of the magneto-optical image at the coordinates. Formula (19) is the X-direction center difference. Formula (20) is the Y-direction center difference. The difference image is shown in Figure 6. In Figure 6a, only weld defects in the vertical direction can be observed. In Figure 6b, only weld defects in the horizontal direction can be observed. In order to observe the welding defects in different directions at the same time, the difference image of the two directions were weighted and fused. As shown in Figure 6c, a differential fusion image with a uniform overall gray intensity was obtained. The spectrum image of the differential fusion image is shown in Figure 6d. Comparing Figure 6d with Figure 5b, it can be found that the difference operation can effectively reduce the influence of noise on the contour information.

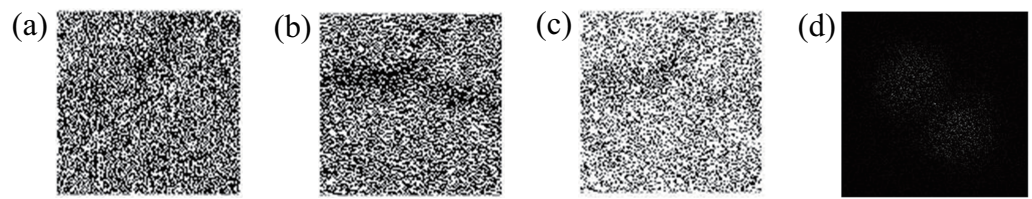


**Figure 6.** Difference image of crack 1. (a) X-direction difference image. (b) Y-direction difference image. (c) Differential fusion image. (d) Spectrum after differential fusion.

Contour is the basic feature of defects in magneto-optical images, which contains the location and size of defects and plays an important role in further quantitative analysis of defects. The active contour has been widely used in image segmentation since it was proposed at the end of the last century. The level set method is used to extract the contour of the fusion image. It can be seen from Figure 6c,d that there was much noise in the fused differential image, which seriously affected the further contour extraction. Therefore, it is necessary to filter the fused image. Because the defect contour exists in the high-frequency part of the magneto-optical image, the required contour information can be obtained by suppressing the low frequency and retaining the high frequency. The processing method transforms the original image to the frequency domain through the Fourier transform to obtain the spectrum. Gaussian low-pass filters with different cut-off frequencies  $D_0$  were used to obtain the images of the initialization level set function and evolution process. The Gauss low-pass filtering formula is as follows:

$$H(u, v) = e^{-D^2(u, v)/2D_0^2} \quad (21)$$

where  $D(u, v)$  is the distance between the frequency variable  $(u, v)$  and the center of the spectrum and  $D_0$  is the cut-off frequency.

Through experiments, when the cut-off frequency  $D_0$  of the filter is too small, most of the original effective information in the image will be removed, including the contour of the defect. When  $D_0$  is too large, it will retain too much noise, which makes the filtering effect not ideal. After binarization with the Otsu method, there is much noise. Therefore, the filtering result of  $D_0 = 10$  was chosen as the input of the Otsu method to obtain a suitable binary image for initializing the level set function. After low-pass filtering, the spectrum image was transformed into a spatial image by the inverse Fourier transform. The formula of the inverse Fourier transform is as follows:

$$f(x, y) = \frac{1}{MN} \sum_{u=0}^{M-1} \sum_{v=0}^{N-1} F(u, v) e^{-j2\pi(\frac{ux}{M} + \frac{vy}{N})} \quad (22)$$

where  $x$  is taken in the range of  $0, 1, 2, \dots, i-1$  and  $y$  is taken in the range of  $0, 1, 2, \dots, j-1$ . The filtered image is shown in Figure 7a. In this method, the level set function is defined as the following formula:

$$\varphi(\mathbf{x}) = \begin{cases} -1 & \mathbf{x} \in \text{inside}(C) \\ 0 & \mathbf{x} \in C \\ 1 & \mathbf{x} \in \text{outside}(C) \end{cases} \quad (23)$$

where  $C$  is the initial contour of surface evolution in the level set method. It was obtained by the rough segmentation of the defect area using the Otsu method. The Otsu method was used to find the optimal threshold of the Gaussian low-pass filter image, and then, binary segmentation was performed. The segmentation result is shown in Figure 7b. Although it was possible to approximately segment the defect area in the image, its edge was too smooth to accurately reflect the contour. Therefore, it can only be used to initialize level set functions. Based on Figure 7b, the level set method was used to evolve the initial contour of the welding defects. The level set function has only three values. On the contour curve  $C$ , the value of  $\varphi$  is 0. In the area surrounded by  $C$ , the value of  $\varphi$  is  $-1$ . In the area outside  $C$ , the value of  $\varphi$  is 1.

Figure 7c shows the result of the segmentation curve after surface evolution. Figure 7d shows the result of superimposing the segmentation curve on the original crack 1 magneto-optical image. As shown in Figure 7c,d, the active contour extraction method can obtain a more accurate defect contour.

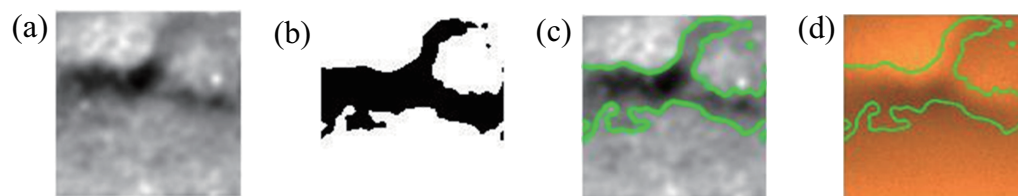


**Figure 7.** Extracting active contour of crack 1 by the level set method. (a) Filtered differential image. (b) Initial contour obtained by binarization. (c) Contour obtained by 41 iterations. (d) Extracted crack 1 final profile.

#### 4. Conclusions

By studying the magneto-optical images of spot welding radial cracks under different magnetic fields, it was found that the magneto-optical images of defects under the VCMF are clearer and more complete. The magneto-optical imaging test showed that under a single magnetic field (CMF and AMF), the imaging of radial cracks that are approximately perpendicular to the magnetic pole is clear; the imaging of radial cracks that are approximately parallel with the magnetic pole is not clear, or even impossible. Under the PCMF, the imaging of the radial crack that is approximately perpendicular to the magnetic pole line is clearer than that under a single magnetic field; the imaging of the radial crack that is approximately parallel with the magnetic pole line is also unclear, or even impossible. However, its image is clearer than that under a single magnetic field (CMF, AMF). Under the VCMF, the radial cracks at all angles of laser spot welding can be imaged on the magneto-optical image. Under the RMF, the multi-angle radial cracks on some magneto-optical images cannot be completely imaged, and some magneto-optical images are blurred.

In the process of magneto-optical image processing, the G-channel image can be extracted to extract the features of defects, which can avoid the influence of image saturation on defect information. Even if the defect is imaged on the magneto-optical image, the defect information and noise distribution cannot be distinguished clearly, which will cause some trouble for the defect feature extraction. The difference operation can effectively reduce the influence of noise on the defect information. An image segmentation method based on a local active contour was used to extract the defect contour in the magneto-optical image. At the same time, the Otsu method was used to obtain the initialization level set function of curve evolution, which solved the problem of the local-region-based method being sensitive to the initialization position.

**Author Contributions:** Conceptualization, X.G.; methodology, N.M., M.T. and C.W.; validation, N.M. and Y.Z.; investigation, N.M. and M.T.; resources, X.G.; data curation, N.M., M.T., C.W. and P.P.G.; writing—original draft preparation, N.M., C.W. and P.P.G.; writing—review and editing, X.G. and Y.Z.; visualization, N.M.; supervision, N.M., X.G., Y.Z. and P.P.G.; project administration, X.G.; funding acquisition, X.G. All authors have read and agreed to the published version of the manuscript.

**Funding:** This work was partly supported by the Guangzhou Municipal Special Fund Project for Scientific and Technological Innovation and Development (Grant No. 202002020068).

**Institutional Review Board Statement:** Not applicable.

**Informed Consent Statement:** Not applicable.

**Data Availability Statement:** Not applicable.

**Conflicts of Interest:** The authors declare no conflict of interest.

## References

1. Zhang, Y.; You, D.; Gao, X.; Katayama, S. Online Monitoring of Welding Status Based on a DBN Model During Laser Welding. *Engineering* **2019**, *5*, 671–678. [\[CrossRef\]](#)
2. Gao, P.; Wang, C.; Li, Y.; Cong, Z. Electromagnetic and eddy current NDT in weld inspection: A review. *Insight-Non Test. Cond. Monit.* **2015**, *57*, 337–345. [\[CrossRef\]](#)
3. Gao, X.; Ding, D.; Bai, T.; Katayama, S. Weld-pool image centroid algorithm for seam-tracking vision model in arc-welding process. *IET Image Process.* **2011**, *5*, 410–419. [\[CrossRef\]](#)
4. Zhang, Y.X.; Han, S.W.; Cheon, J.; Na, S.J.; Gao, X.D. Effect of joint gap on bead formation in laser butt welding of stainless steel. *J. Mater. Process. Technol.* **2017**, *249*, 274–284. [\[CrossRef\]](#)
5. Chen, J.; Wang, T.; Gao, X.; Wei, L. Real-time monitoring of high-power disk laser welding based on support vector machine. *Comput. Ind.* **2018**, *94*, 75–81. [\[CrossRef\]](#)
6. Cao, X.; Jahazi, M. Effect of welding speed on butt joint quality of Ti–6Al–4V alloy welded using a high-power Nd: YAG laser. *Opt. Lasers Eng.* **2009**, *47*, 1231–1241. [\[CrossRef\]](#)
7. Wang, L.; Gao, X.; Kong, F. Keyhole dynamic status and spatter behavior during welding of stainless steel with adjustable-ring mode laser beam. *J. Manuf. Process.* **2022**, *74*, 201–219. [\[CrossRef\]](#)
8. Huang, Y.; Gao, X.; Ma, B.; Liu, G.; Zhang, N.; Zhang, Y.; You, D. Optimization of weld strength for laser welding of steel to PMMA using Taguchi design method. *Opt. Laser Technol.* **2021**, *136*, 106726. [\[CrossRef\]](#)
9. Fan, X.; Gao, X.; Zhang, N.; Ye, G.; Liu, G.; Zhang, Y. Monitoring of 304 austenitic stainless-steel laser-MIG hybrid welding process based on EMD-SVM. *J. Manuf. Process.* **2022**, *73*, 736–747. [\[CrossRef\]](#)
10. Taufiqurrahman, I.; Ahmad, A.; Mustapha, M.; Lenggo Ginta, T.; Ady Farizan Haryoko, L.; Ahmed Shozib, I. The Effect of Welding Current and Electrode Force on the Heat Input, Weld Diameter, and Physical and Mechanical Properties of SS316L/Ti6Al4V Dissimilar Resistance Spot Welding with Aluminum Interlayer. *Materials* **2021**, *14*, 1129. [\[CrossRef\]](#)
11. Chu, Q.; Li, W.Y.; Zou, Y.F.; Yang, X.W.; Wang, W.B. Preliminary investigation of a novel process: Synergetic double-sided probeless friction stir spot welding. *Weld. World* **2021**, *65*, 1441–1449. [\[CrossRef\]](#)
12. Sassi, P.; Tripicchio, P.; Avizzano, C.A. A smart monitoring system for automatic welding defect detection. *IEEE Trans. Ind. Electron.* **2019**, *66*, 9641–9650. [\[CrossRef\]](#)
13. Ji, C.; Na, J.K.; Lee, Y.S.; Park, Y.D.; Kimchi, M. Robot-assisted non-destructive testing of automotive resistance spot welds. *Weld. World* **2021**, *65*, 119–126. [\[CrossRef\]](#)
14. Sifa, A.; Baskoro, A.S.; Sugeng, S.; Badruzzaman, B.; Endramawan, T. *Identification of the Thickness of Nugget on Worksheet Spot Welding Using Non Destructive Test (NDT)—Effect of Pressure*; IOP Conference Series: Materials Science and Engineering; IOP Publishing: Bristol, UK, 2018; Volume 306, p. 012009. [\[CrossRef\]](#)
15. Lacki, P.; Wikeckowski, W.; Wieczorek, P. Assessment of joints using friction stir welding and refill friction stir spot welding methods. *Arch. Metall. Mater.* **2015**, *60*, 2297–2306. [\[CrossRef\]](#)
16. Dejans, A.; Kurtov, O.; Van Rymenant, P. Acoustic emission as a tool for prediction of nugget diameter in resistance spot welding. *J. Manuf. Process.* **2021**, *62*, 7–17. [\[CrossRef\]](#)
17. Park, S.H.; Hong, J.Y.; Ha, T.; Choi, S.; Jhang, K.Y. Deep Learning-Based Ultrasonic Testing to Evaluate the Porosity of Additively Manufactured Parts with Rough Surfaces. *Metals* **2021**, *11*, 290. [\[CrossRef\]](#)
18. Deniz, C.; Cakir, M. In-line stereo-camera assisted robotic spot welding quality control system. *Ind. Robot. Int. J.* **2018**, *45*, 54–63. [\[CrossRef\]](#)
19. Guo, H.; Zheng, B.; Liu, H. Numerical simulation and experimental research on interaction of micro-defects and laser ultrasonic signal. *Opt. Laser Technol.* **2017**, *96*, 58–64. [\[CrossRef\]](#)
20. Forejtová, L.; Zavadil, T.; Kolařík, L.; Kolaříková, M.; Vávra, P. Non-destructive inspection by infrared thermography of resistance spot welds used in automotive industry. *Acta Polytech.* **2019**, *59*, 238–247. [\[CrossRef\]](#)
21. Hassler, U.; Gruber, D.; Hentschel, O.; Sukowski, F.; Grulich, T.; Seifert, L. In-situ monitoring and defect detection for laser metal deposition by using infrared thermography. *Phys. Procedia* **2016**, *83*, 1244–1252. [\[CrossRef\]](#)
22. Su, Z.W.; Xia, Y.J.; Shen, Y.; Li, Y.B. A novel real-time measurement method for dynamic resistance signal in medium-frequency DC resistance spot welding. *Meas. Sci. Technol.* **2020**, *31*, 055011. [\[CrossRef\]](#)
23. Wan, X.; Wang, Y.; Zhao, D. Quality monitoring based on dynamic resistance and principal component analysis in small scale resistance spot welding process. *Int. J. Adv. Manuf. Technol.* **2016**, *86*, 3443–3451. [\[CrossRef\]](#)
24. Spurek, M.A.; Luong, V.H.; Spierings, A.B.; Lany, M.; Santi, G.; Revaz, B.; Wegener, K. Relative Density Measurement of PBF-Manufactured 316L and AlSi10Mg Samples via Eddy Current Testing. *Metals* **2021**, *11*, 1376. [\[CrossRef\]](#)
25. Tsukada, K.; Miyake, K.; Harada, D.; Sakai, K.; Kiwa, T. Magnetic nondestructive test for resistance spot welds using magnetic flux penetration and eddy current methods. *J. Nondestruct. Eval.* **2013**, *32*, 286–293. [\[CrossRef\]](#)
26. Vértesy, G.; Tomáš, I. Nondestructive magnetic inspection of spot welding. *NDT E Int.* **2018**, *98*, 95–100. doi:10.1016/j.ndteint.2018.05.001. [\[CrossRef\]](#)
27. Song, N.; Shiga, K.; Sakai, K.; Kiwa, T.; Tsukada, K. Development of a magnetic phase map for analysis of the internal structure of a spot weld. *Electromagn. Nondestruct. Eval. (XIX)* **2016**, *41*, 302. [\[CrossRef\]](#)
28. Liu, J.; Xu, G.; Ren, L.; Qian, Z.; Ren, L. Defect intelligent identification in resistance spot welding ultrasonic detection based on wavelet packet and neural network. *Int. J. Adv. Manuf. Technol.* **2017**, *90*, 2581–2588. [\[CrossRef\]](#)

29. Sifa, A.; Endramawan, T.; Badruzzaman. Identification of the Quality Spot Welding used Non Destructive Test-Ultrasonic Testing: (Effect of Welding Time). *Iop Conf.* **2017**, *180*, 012101. [[CrossRef](#)]
30. Song, Y.; Hua, L.; Wang, X.; Wang, B.; Liu, Y. Research on the detection model and method for evaluating spot welding quality based on ultrasonic A-scan analysis. *J. Nondestruct. Eval.* **2016**, *35*, 4. [[CrossRef](#)]
31. Liu, J.; Xu, G.; Xu, D.; Zhou, G.; Fan, Q. Ultrasonic C-scan detection for stainless steel spot welding based on wavelet package analysis. *J. Wuhan Univ. Technol.-Mater. Sci. Ed.* **2015**, *30*, 580–585. [[CrossRef](#)]
32. Ma, N.; Gao, X.; Wang, C.; Zhang, Y. Optimization of Magneto-Optical Imaging Visualization of Micro-Defects Under Combined Magnetic Field Based on Dynamic Permeability. *IEEE Trans. Instrum. Meas.* **2021**, *70*, 1–9. doi: 10.1109/TIM.2021.3117074. [[CrossRef](#)]
33. Wang, C.; Wang, C.; Gao, X.; Tian, M.; Zhang, Y. Research on Microstructure Characteristics of Welded Joint by Magneto-Optical Imaging Method. *Metals* **2022**, *12*, 258. [[CrossRef](#)]
34. Radtke, U.; Zielke, R.; Rademacher, H.G.; Crostack, H.A.; Hergt, R. Application of magneto-optical method for real-time visualization of eddy currents with high spatial resolution for nondestructive testing. *Opt. Lasers Eng.* **2001**, *36*, 251–268. [[CrossRef](#)]